Strategy to Enhance the Luminescence of Lanthanide Ions Doped $MgWO_4$ Nanosheets through Incorporation of Carbon Dots

Jingbin Huang,[a, b ,‡] Wei Lu,[c, ‡] Jia Wang,[b] Qingfeng Li,[*,b] Boshi Tian,[b] Chunyang Li,[b] Zhenling Wang,[*,a, b] Lin Jin,[*,b] and Jianhua Hao[*,d]

[a]The College of Chemistry and Molecular Engineering, Zhengzhou University, Zhengzhou 450001, P. R. China

[b]The Key Laboratory of Rare Earth Functional Materials and Applications; Henan Key Laboratory of Rare Earth Functional Materials, Zhoukou Normal University, Zhoukou 466001, P. R. China

[c]University Research Facility in Materials Characterization and Device Fabrication, The Hong Kong Polytechnic University, Hong Kong, P. R. China

[d]Department of Applied Physics, The Hong Kong Polytechnic University, Hong Kong, P. R. China

KEYWORDS: $MgWO_4$: Ln^{3+} nanosheets; carbon dots; luminescence enhancement; doping; energy transfer

ABSTRACT: Highly fluorescent nanomaterials have shown great potential application in optics area. However, further improving their fluorescence properties especially for nanomaterials still remains a challenge. Specifically, luminescence of lanthanide (Ln) ions doped two-dimensional (2D) nanosheets is seldom studied. Herein, we have prepared Ln^{3+} (Ln = Eu, Tb) doped $MgWO_4$ nanosheets, and the luminescence properties of these nanosheets are obviously improved through incorporation of fluorescent carbon dots (CDs) onto the surface of $MgWO_4$: Ln^{3+} (CDs@$MgWO_4$: Ln^{3+}) nanosheets. The obtained $MgWO_4$: Ln^{3+} samples have a 2D nanosheet morphology with triclinic phase, and the morphology and phase structure can be maintained after incorporating CDs onto the nanosheets' surface. The obtained $MgWO_4$: Ln^{3+} nanosheets exhibit the emission characteristic of Ln^{3+} under UV light excitation, and the fluorescence property of CDs@$MgWO_4$: Eu^{3+} and CDs@$MgWO_4$: Tb^{3+} nanosheets increases two and seven folds compared to the corresponding samples without incorporation of CDs, respectively. This luminescent enhancement mechanism might be due to the capturing electrons by CDs and existing energy transfer between CDs and luminescent Ln^{3+}. The PL enhancement through introducing CDs provides a simple and environment-friendly strategy for further improving luminescence property of other lanthanide ions doped nanomaterials.

1. INTRODUCTION

Since graphene was first prepared through the Scotch tape exfoliation of graphite in 2004 by Geim's group,[1] the 2D materials have been increasingly extensive researched due to their fascinating properties and promising potential in diverse areas, such as optics, electronics, catalysis, biomedicine and so on.[2-5] Moreover, the unique structure characters and properties of 2D materials also make them readily form functional 2D nanomaterials to expand their scope of applications. Hence, over a surprisingly short period, a large number of graphene-based 2D materials have been systematically investigated,[6,7] and various types of 2D materials have also been discovered. Among them, the transition metal dichalcogenides (TMDs) are the most prominent example, with MoS_2 as its flagship.[8,9] Other new 2D materials have been developed in recent years, for instance graphitic carbon nitride, hexagonal boron nitride and black phosphorus, etc.[10-14] It is hoped that more and more new-type 2D/quasi-2D materials would be developed and thus expanded their application fields. On the other hand, as a wide band gap self-activated luminescent material, $MgWO_4$ exhibits the superior optical, photochemical and photoelectronic performances, which make it be potentially applied in many areas such as scintillation, dielectric ceramic, photovoltaic devices, etc.[15-17] However, $MgWO_4$ with 2D/quasi-2D nanostructure has not been reported till now, furthermore, there are only few literatures about lathanide (Ln) ions doped $MgWO_4$ and the luminescent properties of these materials are not systematically investigated. For instance, Eu^{3+} doped $MgWO_4$ nanoparticles were synthesized as a red phosphor,[18] Er^{3+}/Yb^{3+} co-doped $MgWO_4$ rod-like grains were reported, presenting dual-mode emission and temperature sensing properties,[19] 3D flower-like $MgWO_4$: Eu^{3+} hierarchical structures were prepared, exhibiting fluorescence enhancement through introduction of carbon dots.[20]

In general, lanthanide ions doped nanomaterials often suffer from lower luminescence quantum efficiency due to their surface defects, low molar absorptivity, narrow absorption band, etc.[21,22] The luminescence properties of lanthanide ions doped $MgWO_4$ with 2D/quasi-2D nanostructure might be mainly affected by the surface defects because of its thickness at nanoscale. Some viable methods have been used to enhance the luminescence property of lanthanide ions doped nanomaterials. For example, sensitizing $GdVO_4$: Ln^{3+} by organic ligands,[23] forming core/shell structure on the luminescence,[24, 25] plasmonic enhancement of upconversion luminescence and so on.[26-28] It is known that carbon dots as a kind of new functional materials possess lots of excellent properties, such as hypotoxicity, chemical durability, good biocompatibility, etc.,[29,30] it can be widely applied for various fields for example imaging,

biosensing, optoelectronic devices, drug delivery, photocatalysis and so on.[31-37] The investigations have confirmed that the combination of CDs with other materials could prominently enhance the performance of the original materials, such as Li-ion storage of TiO_2 nanoribbon,[38] NO_2 sensing performance of reduced graphene oxide,[39] photocatalytic activity of WS_2,[40] mechanical properties of hyperbranched epoxy,[41] multifunctional properties of composite materials,[42] etc. However, there are rarely literatures to enhance the fluorescence performances of lanthanide ions doped nanomaterials through using CDs (e.g., Eu^{3+} doped LaF_3-CDs nanocomposites[43] and CDs@$MgWO_4$: Eu^{3+} hierarchical structures[20]).

In our previous work, we have prepared 3D flower-like $MgWO_4$: Eu^{3+} hierarchical structures, discussed the growth mechanism of flower-like morphology, and found the luminescent enhance phenomenon of $MgWO_4$: Eu^{3+} flowers through incorporation of fluorescent carbon dots (CDs).[20] In this work, $MgWO_4$: Ln^{3+} (Ln = Eu, Tb) nanosheets were successfully synthesized by a simple hydrothermal method. The phase structure, morphology and fluorescence performances were investigated and the synthesis conditions of $MgWO_4$: Ln^{3+} nanosheets were optimized. The variety and concentration of the doping Ln^{3+} ions have little effect on the nanosheet morphology and phase structure of the obtained samples. Interestingly, the photoluminescence (PL) properties of the obtained $MgWO_4$: Ln^{3+} nanosheets could be obviously enhanced by introducing CDs onto the surface of nanosheets to form CDs@$MgWO_4$: Ln^{3+} nanosheets. Compared to the $MgWO_4$: Eu^{3+} and $MgWO_4$: Tb^{3+} nanosheets, the PL emission intensities of CDs@$MgWO_4$: Eu^{3+} and CDs@$MgWO_4$: Tb^{3+} nanosheets increased two and seven folds, respectively. The combination process between CDs and $MgWO_4$: Ln^{3+} (Ln = Eu, Tb) nanosheets was analyzed based on FTIR and XPS analysis, TEM and HRTEM images, SAED patterns, etc. The luminescent enhancement mechanism was discussed according to the energy levels of Ln^{3+} ions and CDs. This investigation develops a synthesis technique for new 2D materials, and provides a feasible strategy for improving luminescence property of Ln^{3+} ions doped nanomaterials as well.

2. EXPERIMENTAL SECTION

2.1. Materials. All chemicals were used without further purification. $Mg(NO_3)_2{\cdot}6H_2O$ (Analytical reagent, AR, 99.0%) was obtained from Zhengzhou Spake Technology Co., Ltd, China; $Na_2WO_4{\cdot}2H_2O$ (AR, 99.5%) was acquired from Tianjin Basf Chemical Co., Ltd, China; Citric acid (AR, 99.8%) and urea (AR, 99.0%) were purchased from Tianjin Kaitong Chemical Reagent Co., Ltd, China; $Eu(NO_3)_3{\cdot}6H_2O$ (AR, 99.9%) and $Tb(NO_3)_3{\cdot}5H_2O$ (AR, 99.9%) were purchased from Aladdin Chemicals.

2.2. Preparation of $MgWO_4$: Ln^{3+} (Ln = Eu, Tb) Nanosheets. $MgWO_4$: Ln^{3+} (Ln = Eu, Tb) nanosheets were synthesized by a simple hydrothermal method. First, a total amount (1.0 mmol) of $Mg(NO_3)_2{\cdot}6H_2O$ and $Eu(NO_3)_3{\cdot}6H_2O$/$Tb(NO_3)_3{\cdot}5H_2O$ with a desired molar ratio were dissolved in 10.0 mL of distilled water to form a clear solution, and then 20.0 mL of aqueous solution containing 1.0 mmol of $Na_2WO_4{\cdot}2H_2O$ was added into the above solution, and the obtained mixture was continuously stirring for 15 min. Subsequently, the prepared suspension was transferred into a 50 mL of Teflon-lined stainless autoclave, and the autoclave was sealed and maintained at 180 °C for 12 h. After heating, the autoclave was cooled to room temperature, and the obtained white precipitate was washed using distilled water and ethanol for several times. Finally, the samples were dried at 80 °C for 12 h to obtain $MgWO_4$: Ln^{3+} (Ln = Eu, Tb) nanosheets.

2.3. Preparation of CDs@$MgWO_4$: Ln^{3+} (Ln = Eu, Tb) Nanosheets. CDs were prepared according to a previous reported method, using citric acid as the carbon source in the presence of urea.[44] The fabrication of CDs@$MgWO_4$: Ln^{3+} (Ln = Eu, Tb) nanosheets is similar to $MgWO_4$: Ln^{3+} (Ln = Eu, Tb) nanosheets. Before the prepared suspension was transferred into a 50 mL of Teflon-lined stainless autoclave, the different amount of 0.029 g mL^{-1} CDs solution was added into the suspensions and stirred for a given time, respectively. Then the mixture containing CDs was transferred into a 50 mL of Teflon-lined stainless autoclave, and the other procedure is similar to mentioned above.

2.4. Characterizations. The X-ray powder diffraction (XRD, Bruker D8) was used to characterized the phase structure of the obtained samples under a scanning rate of 6°/min with Cu Kα radiation (λ = 0.154056 nm). The morphology and energy dispersive X-ray spectroscopy (EDX) were observed using scanning electron microscope (SEM) (FEI Quanta 200). The bright field TEM image and selected area electron diffraction (SAED) pattern were obtained by a JEOL-2011 transmission electron microscope at an acceleration voltage of 200 kV. PL spectra and lifetime were recorded using an FLS920P Edinburgh Analytical Instrument apparatus equipped with a 450 W xenon lamp, a μF900H high-energy micro-second flash lamp and a 360 nm laser diode as the excitation sources. The quantum efficiency (QE) was measured by an integrating sphere whose inner face was coated with BenFlect equipped with a spectrofluorometer. The slit widths for the excitation and emission were 5.0 and 0.2 nm, respectively. The step size was 0.2 nm and the integration time was 0.3 seconds. Fourier transform infrared spectroscopy (FTIR) was carried out within KBr slices in the 4000-400 cm^{-1} range using a Nexus 912 AO446 infrared spectrum radiometer. X-ray photoelectron spectroscopy (XPS) measurements were performed using a Thermo Scientific Escalab 250 spectrometer (Escalab 250Xi) operated at 120 W. UV-vis diffuse reflectance spectra (DRS) were recorded at room temperature using a UV-2600 spectrophotometer.

3. RESULTS AND DISCUSSION

3.1. $MgWO_4$: Ln^{3+} (Ln = Eu, Tb) Nanosheets. The morphology and phase structure of the obtained $MgWO_4$: Ln^{3+} (Ln = Eu, Tb) nanosheets were analyzed by SEM, TEM and XRD technique. The SEM images of the representative $MgWO_4$: 5%Eu^{3+} sample is shown in Figure 1a and Figure 1b. It is found that $MgWO_4$: 5%Eu^{3+} sample is consisted of thin nanosheets with the length and width at micron scale and the thickness of about 25 nm. When Eu^{3+} doping concentration was gradually changed from 1% to 15%, the thin nanosheet morphology of $MgWO_4$: Eu^{3+} samples can be maintained except for the $MgWO_4$: 15%Eu^{3+} sample with slightly thicker thickness (Figure S1). The phenomenon that the thin nanosheet morphology can be kept with changing the doping concentration from 1% to 10% is similar to that of $MgWO_4$: xTb^{3+} samples, as shown in Figure S2. This indicated that the variety and doping concentration (below 15%) of the doped rare earth ions have little influence on the morphology of $MgWO_4$: Ln^{3+} nanosheets. The XRD results of $MgWO_4$: Eu^{3+} nanosheets with various doping concentrations were given in Figure S3. The results indicated that the as-prepared $MgWO_4$: Eu^{3+} nanosheets are mainly composed of triclinic phase structure of $MgWO_4$, and the diffraction peaks of these samples with the different Eu^{3+} doping concentrations are consistent with the standard card of $MgWO_4$ (PDF# 45-0412). This suggested that the phase structure of $MgWO_4$: Eu^{3+} nanosheets is almost not affected by the doping concentration of Eu^{3+} ions. As expected, the variety of doped Ln^{3+} has also less effect on the phase structure of $MgWO_4$: Tb^{3+} nanosheets, which can be seen from the XRD results of $MgWO_4$: Tb^{3+} nanosheets (Figure S4). In the triclinic structure of Ln^{3+} (Ln = Eu, Tb) doped $MgWO_4$, the ionic radii of Eu^{3+} (0.0947 nm) and Tb^{3+} (0.0923 nm) ions are adjacent to that of Mg^{2+} (0.072 nm) ions with 6 CN (CN = coordination number). Hence, Eu^{3+} and Tb^{3+} ions are very likely to substitute for Mg^{2+}

ions in $MgWO_4$ crystal. Considering the different oxidation states of doping Ln^{3+} and Mg^{2+} ions, the Ln^{3+} ions would adopt the charge non-equivalently substituting for the Mg^{2+} sites, and the positive charge would be excess in the host lattice of $MgWO_4$, which makes charge compensation necessary. One possible charge compensating pattern is $2Ln^{3+}$ (Ln = Eu, Tb) ions substituting for $3Mg^{2+}$ ions to create $2Ln^{\circ}_{Mg}$ positive defects and $V^{''}_{Mg}$ negative defect: $2Ln^{3+} + 3Mg^{2+} \rightarrow 2Ln^{\circ}_{Mg} + V^{''}_{Mg}$. [45, 46] As a consequence, the oxygen ions adjacent to the Mg^{2+} ions might slight deviate from the initial lattice sites in $MgWO_4$ crystals structure.[46]

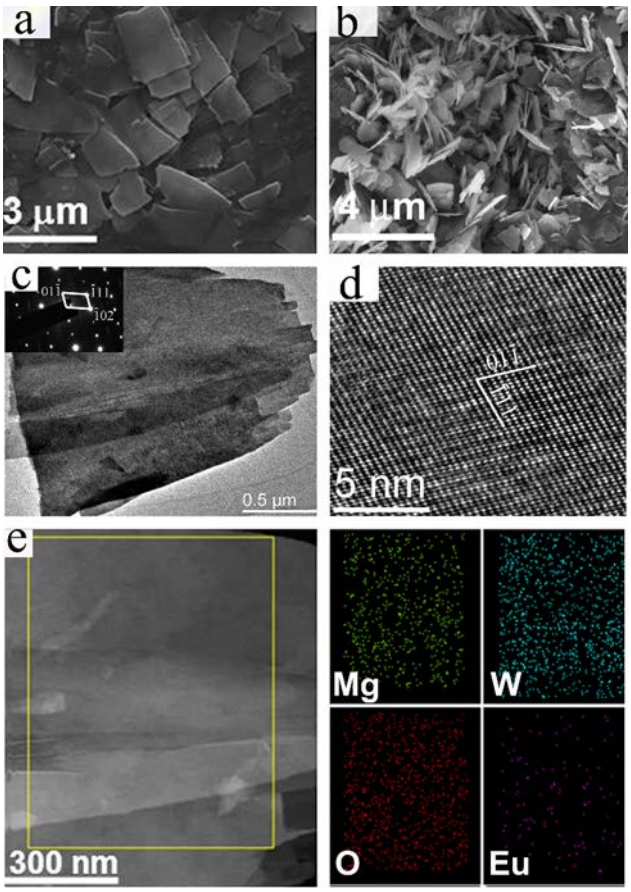

Figure 1. (a, b) SEM images, (c) TEM and (d) HRTEM images and SAED pattern (c, inset) of $MgWO_4$: Eu^{3+} nanosheets. (e) The STEM-HAADF image of an individual $MgWO_4$: Eu^{3+} nanosheet and EDS element mappings of Mg, W, O and Eu elements.

To investigate the microstructure of the obtained $MgWO_4$: Ln^{3+} (Ln = Eu, Tb) nanosheets, the representative $MgWO_4$: 5%Eu^{3+} nanosheets were observed by TEM image (Figure 1c), It is found that the $MgWO_4$: 5%Eu^{3+} sample displays a thin nanosheet like other 2D materials (graphene, MoS_2, etc.). The corresponding SAED pattern in the left inset obtained from an individual nanosheet gives a clear periodic arranged diffraction pattern, and can be indexed to the (01-1), (-111) and (-102) planes of $MgWO_4$ with triclinic phase structure. The HRTEM image of $MgWO_4$: 5%Eu^{3+} nanosheet (Figure 1d) exhibits a single crystalline feature, and the values of interplanar spacings are 0.626 and 0.358 nm, which are assigned to the (01-1) and (-111) planes of $MgWO_4$. The STEM-HAADF images (Figure 1e) shows the morphology of an individual $MgWO_4$: Eu^{3+} nanosheet. The EDS elemental mappings indicate that obtained nanosheets are consisted of Mg, W, O and Eu elements. As for $MgWO_4$: Tb^{3+} nanosheets, the morphology and single crystalline feature, SAED patterns, STEM-HAADF, and EDS elemental mappings are similar to that of $MgWO_4$: Eu^{3+} nanosheets, as given in Figure S5.

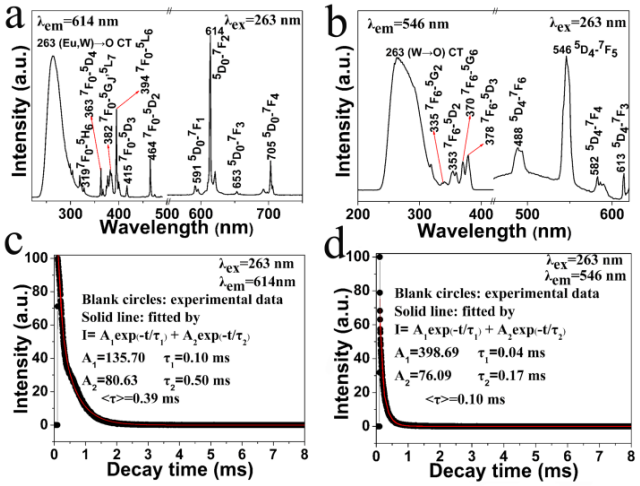

Figure 2. PL excitation (left) and emission (right) spectra of (a) $MgWO_4$: Eu^{3+} and (b) $MgWO_4$: Tb^{3+} nanosheets, and the luminescent decay curves of (c) $MgWO_4$: Eu^{3+} and (d) $MgWO_4$: Tb^{3+} nanosheets.

The as-prepared $MgWO_4$: Ln^{3+} (Ln = Eu, Tb) nanosheets exhibited the characteristic emission of the doping rare earth ions under ultraviolet light. To further compare the difference in optical properties of $MgWO_4$ nanosheets and 3D flower-like $MgWO_4$ hierarchical structures (in our previous report) with the same doping concentrations of Eu^{3+}, the luminescent intensities and luminescence decay curves were investigated, as shown in Figure S6. It is found that 3D flower-like $MgWO_4$: 5%Eu^{3+} shows a stronger emission intensity than that of the $MgWO_4$: 5%Eu^{3+} nanosheets under the different excitation of 263 nm (Figure S6a) and 394 nm (Figure S6b) UV light. The decay curves for these two samples can be fitted into a double exponential behavior (Figure S6c, Figure S6d) and a single exponential behavior (Figure S6e, Figure S6f) under the excitation of 263 and 394 nm UV light. The values of lifetime of $MgWO_4$: 5%Eu^{3+} nanosheets (Figure S6c, 0.33 ms; Figure S6e, 0.27 ms) are smaller than that of 3D flower-like $MgWO_4$: 5%Eu^{3+} hierarchical structures (Figure S6d, 0.44 ms; Figure S6f, 0.36 ms).

As mentioned above, the nanosheet morphology and phase structure of $MgWO_4$: Ln^{3+} (Ln = Eu, Tb) samples were almost not affected by the doping concentration of Ln^{3+}, whereas their luminescence properties were obviously affected by the doping concentration. The amount of defects come from the substitution of doped Ln^{3+} for Mg^{2+} would be gradually increased with increasing of Ln^{3+} doping concentrations, so their luminescence properties must be affected by the amount of defects that might be acted as the luminescence quenching centers. The PL emission spectra of $MgWO_4$: x%Eu^{3+} (x=0, 1, 3, 5, 8, 10, 12, 15) nanosheets under the excitation of 263 nm UV light as shown in Figure S7a. It is found that the emission intensities increases gradually with increasing of Eu^{3+} doping concentrations, reaches a maximum at 12%, and then decreases. However, the opposite results can be observed in WO_4^{2-} groups at 490 nm as shown in Figure S7b. The changing trend of the PL emission spectra of $MgWO_4$: Tb^{3+} nanosheets is similar to $MgWO_4$: Eu^{3+} nanosheets, except for reaching a maximum at 8% (Figure S7c). The emission intensity of $MgWO_4$: Ln^{3+} (Ln = Eu, Tb)

nanosheets firstly increases with increasing of doping concentration is mainly due to the increase of luminescent centers, though the amount of defects as luminescence quenching increase simultaneously which might not act the main role. The decreasing of the emission intensity after reaching a maximum with further increasing the doping concentration might be attributed to the concentration quenching effect and the increasing defects when Eu^{3+} and Tb^{3+} at relatively higher doping concentrations.[24]

In the subsequent discussion, the $MgWO_4$: 12%Eu^{3+} and $MgWO_4$: 8%Tb^{3+} nanosheets with optimized luminescence properties were selected as the representative samples to investigate the luminescence properities, formed composite, luminescence enhancement effect and so on. Figure 2a gives the PL excitation and emission spectra of the representative $MgWO_4$: 12%Eu^{3+} nanosheets, the excitation spectrum (Figure 2a, left) contains a broad band excitation peak at 263 nm is attributed to the absorption of WO_4^{2-} group and charge transfers of (Eu, W-O).[47] The sharp excitation peaks are assigned to the $^7F_0$-$^5H_6$ (319 nm), $^7F_0$-$^5D_4$ (363 nm), $^7F_0$-$^5L_7$,^5G_J (382 nm), $^7F_0$-$^5L_6$ (394 nm), $^7F_0$-$^5D_3$ (415 nm), and $^7F_0$-$^5D_2$ (464 nm) transitions of Eu^{3+} ions, respectively.[48] The emission spectrum (Figure 2a, right) excited at 263 nm shows characteristic emission peaks of Eu^{3+} ($^5D_0$-$^7F_1$, $^7F_2$, $^7F_3$, $^7F_4$) with wavelength ranging from 500 to 750 nm.[49] As for $MgWO_4$: Tb^{3+} nanosheets, the PL excitation and emission spectra of the representative $MgWO_4$: 8%Tb^{3+} nanosheets were given in Figure 2b (left) and (right), respectively. It is observed from Figure 2b (left) that the excitation spectrum also contains a broad band excitation peak, which is assigned to WO_4^{2-} absorption and W-O charge transfers (CT),[50] and other excitation peaks belongs to $^7F_6$-$^5G_2$ (335 nm), $^7F_6$-$^5D_2$ (353 nm), $^7F_6$-$^5G_6$ (370 nm) and $^7F_6$-$^5D_3$ (378 nm) transitions of Tb^{3+} ions.[51] The PL emission spectrum corresponds to the characteristic emission $^5D_4$-$^7F_6$ (490 nm), $^5D_4$-$^7F_5$ (546 nm), $^5D_4$-$^7F_4$ (587 nm) and $^5D_4$-$^7F_3$ (622 nm) of Tb^{3+} ions.[51]

In addition, the PL spectra of undoped $MgWO_4$ nanosheets is measured as shown in Figure S8a, and they are composed of broad excitation and emission bands with maximum at 263 nm (Figure S8a, left) and 490 nm (Figure S8a, right), respectively. The luminescence decay curves of undoped $MgWO_4$ host materials and $MgWO_4$: Ln^{3+} (Ln = Eu, Tb) nanosheets (λ_{ex} = 263 nm, λ_{em} = 490 nm) can be well fitted into a single exponential function. However, the lifetime values of $MgWO_4$: 12%Eu^{3+} nanosheets (Figure S8c, 4.8 μs) and $MgWO_4$: 8%Tb^{3+} nanosheets (Figure S8d, 5.4 μs) are shorter compared to the undoped $MgWO_4$ nanosheets (Figure S8b, 11.14 μs), suggesting the energy transfer from WO_4^{2-} to the doping Ln^{3+}. It can be seen that the luminescent decay curves of $MgWO_4$: 12%Eu^{3+} (Figure 2c, λ_{ex} = 263 nm, λ_{em} = 614 nm) and $MgWO_4$: 8%Tb^{3+} (Figure 2d, λ_{ex} = 263 nm, λ_{em} = 546 nm) nanosheets are well fitted into a double exponential function as shown in equation (1),[52] which is derived from the energy transfer between different luminescence centers (WO_4^{2-} groups and doping Ln^{3+}).

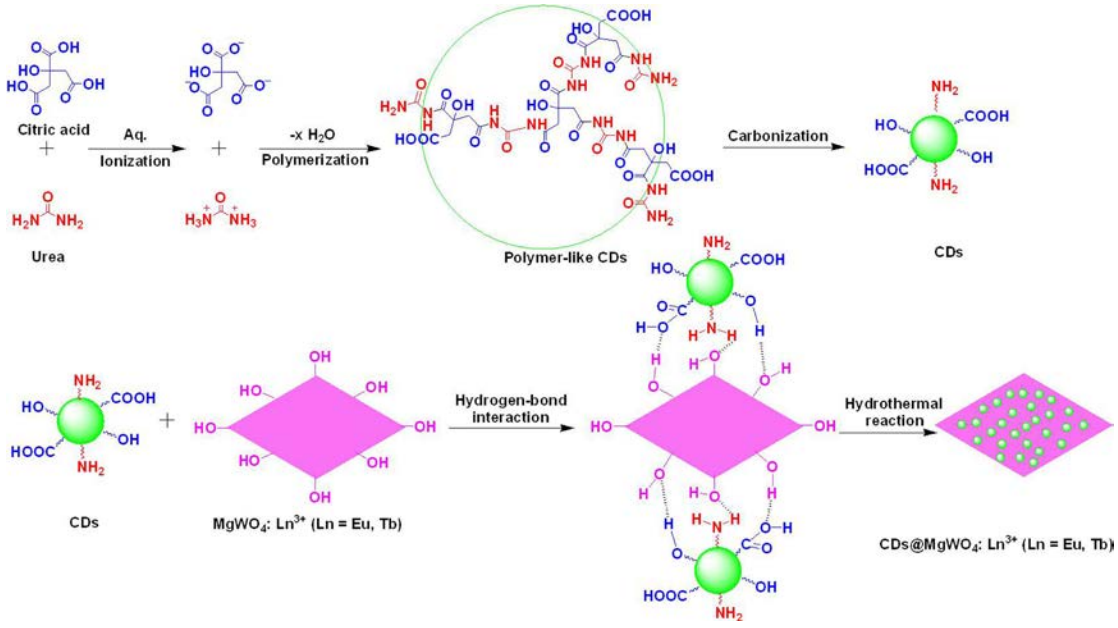

Figure 3. Schematic illustration of the synthesis of CDs and the formation process of CDs@$MgWO_4$: Ln^{3+} (Ln = Eu, Tb) nanosheets.

$$I = A_1 \exp(-t/\tau_1) + A_2 \exp(-t/\tau_2) \quad (1)$$

Where I is the emission intensity; τ_1 and τ_2 are the fast and slow components of the luminescent lifetime, respectively; A_1 and A_2 are the corresponding fitting parameters. The average lifetime can be determined by the formula according to equation (2).[51]

$$\tau = (A_1\tau_1^2 + A_2\tau_2^2)/(A_1\tau_1 + A_2\tau_2) \quad (2)$$

Through the fitting calculation, the average lifetimes of $MgWO_4$: 12%Eu^{3+} and $MgWO_4$: 8% Tb^{3+} nanosheets are 0.39 and 0.10 ms, respectively.

3.2. CDs@$MgWO_4$: Ln^{3+} (Ln = Eu, Tb) Nanosheets. To further enhance the luminescent performance of $MgWO_4$: Ln^{3+} nanosheets, the fluorescent CDs were incorporated onto $MgWO_4$: Ln^{3+} nanosheets to form CDs@$MgWO_4$: Ln^{3+} nanosheets. The diagram of the formation process of CDs and CDs@$MgWO_4$: Ln^{3+} (Ln = Eu, Tb) nanosheets were shown in Figure 3.

Firstly, CDs were synthesized by same method in our previous report.[20] The XRD pattern of the obtained CDs shown in Figure 4a is composed of a broad peak centered at 2θ = 25.6°, which is the characteristic peak of amorphous phase CDs.[53] The

PL spectra of the obtained CDs were given in Figure 4b. The excitation (Figure 4b, left) and emission (Figure 4b, right) spectra are composed of a broad band with a maximum at 440 nm and 510 nm. This is a typical luminescence characters of CDs, and the broad excitation and emission spectra are mostly related to the surface states of CDs.[54,55] The TEM image of the obtained CDs (Figure 4c) displays a uniform and dispersed spherical particles with the size around 3-5 nm. And the HRTEM image (Figure 4d) shows that lattice spacing of CDs is about 0.32 nm, which is consistent with the (002) plane of carbon dots.

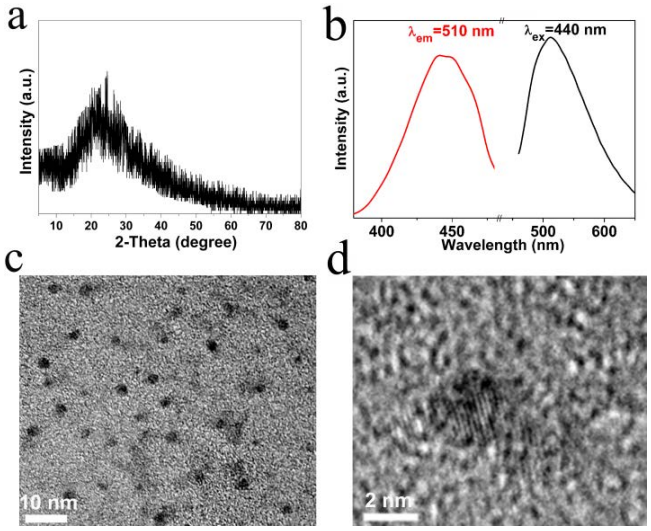

Figure 4. (a) XRD pattern, (b) PL excitation and emission spectra, (c) TEM and (d) HRTEM images of the as-prepared CDs.

From the synthesis procedure of CDs (Figure 3), it was found that citric acid and urea were ionized in the solution firstly, then they formed polymer-like CDs by dehydration-condensation reaction.[44] Finally, the CDs were formed from polymer-like CDs through the carbonization process. Hence, the obtained CDs have abundant –OH, –COOH, $–NH_2$, etc. functional groups on its surfaces, this can be confirmed by FTIR spectrum (Figure 5a) that will be discussed in subsequent section. It is these functional groups that could provide driving force for the combination of CDs with $MgWO_4$: Ln^{3+} nanosheets. As shown in Figure 3, the suspension of $MgWO_4$: Ln^{3+} precursors was mixed with the solution of CDs. The functional groups including –OH, –COOH, $–NH_2$ on the CDs' surface would be combined with –OH groups on the surface of $MgWO_4$: Ln^{3+} precursors. After hydrothermal treatment, the CDs were incorporated onto the surface of $MgWO_4$: Ln^{3+} nanosheets to form CDs@$MgWO_4$: Ln^{3+} nanosheets finally.

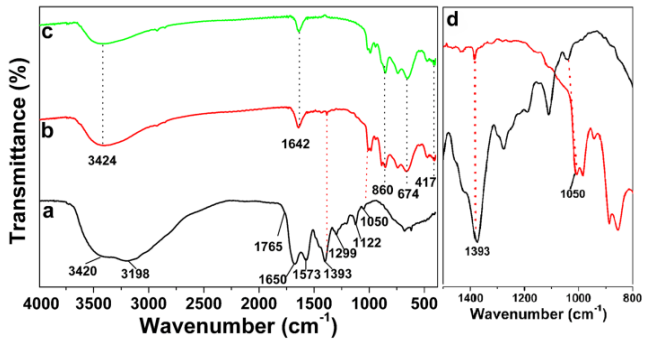

Figure 5. FTIR spectra of (a) CDs, (b) CDs@$MgWO_4$: Eu^{3+} nanosheets, (c) $MgWO_4$: Eu^{3+} nanosheets and (d) the magnified area of Figure 5a and Figure 5b in the range of 1500-800 cm^{-1}.

The combination of CDs with $MgWO_4$: Ln^{3+} nanosheets can be directly/indirectly confirmed by FTIR, TEM, HRTEM, SAED pattern, XPS, PL spectrum. The FTIR spectra of CDs as shown in Figure 5a, The peaks located at 3420 cm^{-1} and 3198 cm^{-1} are assigned to the vibrations of –OH and N–H.[56] The stretching vibrations of C=O (from –COOH) and C–O can be identified by the peaks at (1765 , 1650 cm^{-1}) and (1299, 1050 cm^{-1}), respectively.[57] The other vibration peaks at 1393, 1122 and 1573 cm^{-1} belong to C–O–C, C–NH–C and N–H groups, respectively.[58] This reveals that the negatively charged carboxyl and hydroxyl groups are mainly functional groups in obtained CDs. The FTIR spectrum OF $MgWO_4$: 12%Eu^{3+} nanosheets (Figure 5c) shows the typical absorption features of $MgWO_4$, the absorption peaks at 417, 674 and 860 cm^{-1} are assigned to the (Mg–O, O–W–O, W–O) bond stretching, respectively.[59] When CDs were combined with $MgWO_4$: 12%Eu^{3+} nanosheets to form CDs@$MgWO_4$: 12%Eu^{3+} nanosheets, the FTIR spectrum shown in Figure 5b still exhibits the typical absorption features of $MgWO_4$. The two peaks at (3424, 1642 cm^{-1}) can be ascribed to the –OH vibration from remaining crystalline water.[60] From the magnified image (Fig 5d) in the range of 1500-800 cm^{-1}, there are two similar peaks at 1393 and 1050 cm^{-1} existing in the FTIR spectra of CDs and CDs@$MgWO_4$: 12%Eu^{3+} nanosheets. Hence, to some extent, this result suggests that the CDs have been incorporated onto $MgWO_4$: 12%Eu^{3+} nanosheets.

The combination of CDs and $MgWO_4$: Ln^{3+} nanosheets could be direct confirmed by TEM technique. Figure 6 showed the TEM images, SAED patterns, HRTEM images of $MgWO_4$: 8%Tb^{3+} nanosheets (left) and CDs@$MgWO_4$: 8%Tb^{3+} nanosheets (right). It is found that there are many black dots (CDs) on the nanosheet for CDs@$MgWO_4$: Tb^{3+} sample (Figure 6d), and the average size of these CDs is around 3.8 nm, the size is in agreement with the obtained CDs (Figure 4c). Comparing to TEM image of $MgWO_4$: Tb^{3+} nanosheets (Figure 6a), it indicates that the CDs have been incorporated onto $MgWO_4$: Tb^{3+} nanosheets. The SAED pattern of single $MgWO_4$: Tb^{3+} nanosheets (Figure 6b) should be assigned to the

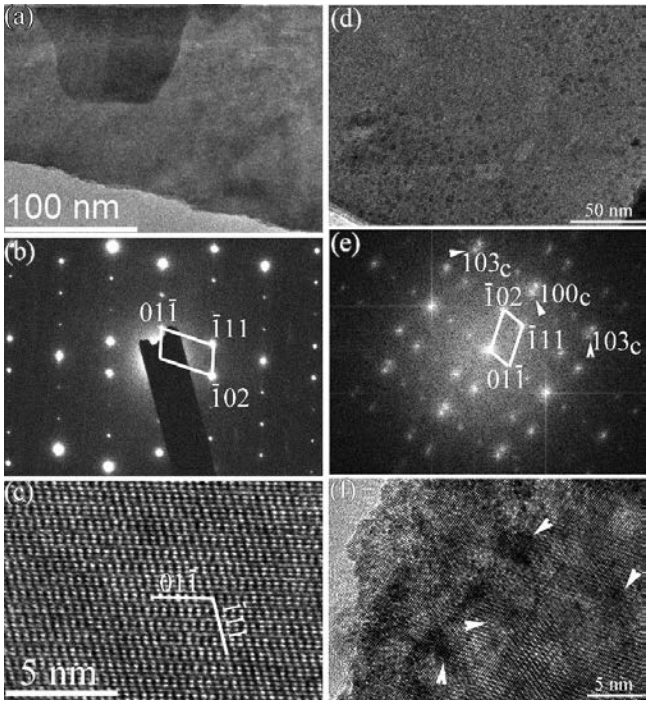

Figure 6. (a, d) TEM images, (b, e) SAED patterns, (c, f) HRTEM images of $MgWO_4$: Tb^{3+} nanosheets (left) and CDs@$MgWO_4$: Tb^{3+} nanosheets (right).

(01-1), (-111) and (-102) planes of $MgWO_4$ crystal with triclinic phase structure, which is consistent with the XRD results. As for CDs@$MgWO_4$: Tb^{3+} nanosheets, the SAED pattern (Figure 6e) includes both of the (01-1), (-111) and (-102) planes of $MgWO_4$ crystal and the (100) and (103) planes of CDs (denoted by arrows). This result also proves the incorporation of CDs onto the surface of $MgWO_4$: Tb^{3+} nanosheets. The HRTEM image of $MgWO_4$: Tb^{3+} nanosheet (Figure 6c) exhibits a single crystalline feature, and the values of interplanar spacings are 0.626 and 0.358 nm, which are identical to the (01-1) and (-111) facet distance of bulk $MgWO_4$ powders, respectively. From the HRTEM image of CDs@$MgWO_4$: Tb^{3+} nanosheet (Figure 6f), besides the planes of $MgWO_4$: Tb^{3+} nanosheet, the planes of CDs can also be clearly observed, as denoted by arrows. For $MgWO_4$: 12%Eu^{3+} nanosheets, the CDs could be incorporated onto the surface of $MgWO_4$: Eu^{3+} nanosheets to form CDs@$MgWO_4$: Eu^{3+} nanosheets as well. This can be confirmed by TEM technique, as shown in Figure S9.

To further investigate the incorporation of CDs onto the surface of $MgWO_4$: Ln^{3+} nanosheets, the surface chemical compositions of the representative CDs@$MgWO_4$: 12%Eu^{3+} nanosheets were analyzed by X-ray photoelectron spectroscopy (XPS). As shown in Figure 7a, the full range XPS spectrum is composed of the peaks at 37, 285, 400, 532, 1164, and 1303 eV, which are attributed to W 4f , C 1s, N 1s , O 1s, Eu 3d and Mg 1s, respectively. The high-resolution XPS of C 1s (Figure 7b) can be divided into three main peaks at 283.6, 285.1, and 287.5 eV, associated with C–C (sp^2–C), C–O (oxygen in hydroxyl), and C=O (carboxyl) groups, respectively.[61,62] The three peaks at 532.8, 531.4 and 530.2 eV in the high-resolution XPS of O 1s (Figure 7c) can be assigned to C–O, C=O and O–metal (bond to magnesium and tungsten atoms, Mg–O, W–O).[59] This analysis indicates that there are still plenty of hydroxyl and carboxyl groups on the surface of CDs@$MgWO_4$:

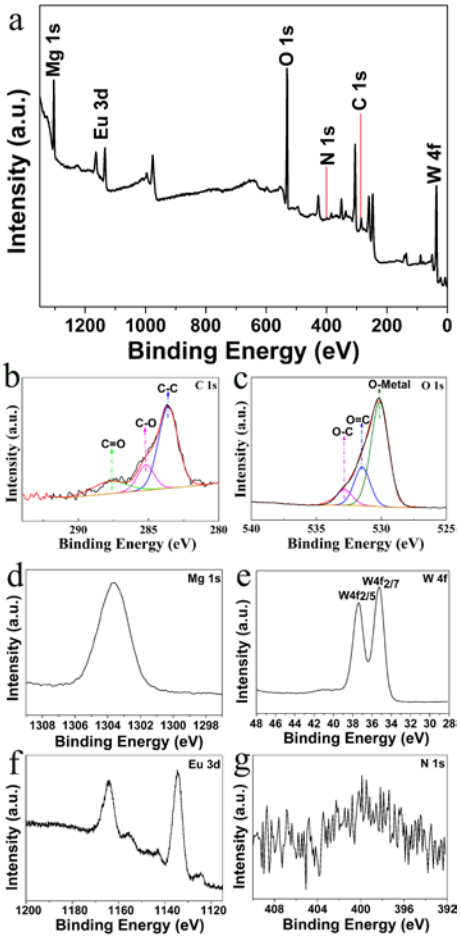

Figure 7. (a) XPS spectrum of CDs@$MgWO_4$: Eu^{3+} nanosheets and the corresponding high-resolution XPS spectra of (b) C 1s, (c) O 1s, (d) Mg 1s, (e) W 4f, (f) Eu 3d and (g) N 1s.

12%Eu^{3+} nanosheets, confirming the successful incorporation of CDs onto $MgWO_4$: Eu^{3+} nanosheets, which is consistent with the results of FTIR spectra (Figure 5). In addition, the peak at 1303.66 eV (Figure 7d) is related to Mg 1s,[63] and the peaks at 35.25 and 37.42 eV (Figure 7e) are assigned to W $4f_{2/7}$ and W $4f_{2/5}$,[64] respectively. The high-resolution XPS of Eu 3d (Figure 7f) has two peaks: the peak around 1134.4 eV corresponds to Eu^{3+} $3d_{5/2}$, and the peak at 1164.1 eV is a satellite peak.[65] The weak peak at 399.9 eV corresponds to N 1s (Figure 7g).[66] For CDs@$MgWO_4$: 8%Tb^{3+} nanosheets, the full range XPS and the corresponding high-resolution XPS of C 1s (284.8 eV), O 1s (530.4 eV), Mg 1s (1303.8 eV), W 4f (37 eV), Tb 3d (1242.1 eV) and N 1s (397.4 eV) were shown in Figure S10.

3.3. The Luminescence Enhancement Effect and Enhanced Mechanism. The incorporation of CDs onto the surface of $MgWO_4$: Ln^{3+} nanosheets to form CDs@$MgWO_4$: Ln^{3+} nanosheets could prominently enhance the luminescence properties of these original nanosheets. Figure 8a showed the PL excitation spectra of $MgWO_4$: 12%Eu^{3+} nanosheets (black line) and CDs@$MgWO_4$: 12%Eu^{3+} nanosheets (red line). It can be seen that the excitation spectrum intensity of CDs@$MgWO_4$: 12%Eu^{3+} nanosheets is obviously increased compared with that of $MgWO_4$: 12%Eu^{3+} nanosheets for both of the broad excitation band (Eu-O and W-O charge transfers) and the sharp excitation peaks of Eu^{3+} ions. It can be observed from the PL emission spectra (Figure 8b) that the emission intensity (614 nm) of CDs@$MgWO_4$: 12%Eu^{3+} nanosheets

(red line) increases more than 2.5 times than that of $MgWO_4$: 12%Eu^{3+} nanosheets (black line). Correspondingly, under the irradiation of 263 nm UV light, the luminescence photograph of CDs@$MgWO_4$: 12%Eu^{3+} nanosheets (insets, right) is obviously stronger than that of $MgWO_4$: 12%Eu^{3+} nanosheets (insets, left) by naked eyes. The photoluminescence quantum yield increases from 9.07% for $MgWO_4$: 12%Eu^{3+} nanosheets without incorporation of CDs to 10.65% for CDs@$MgWO_4$: 12%Eu^{3+} nanosheets. Under the excitation of 394 nm UV light (Eu^{3+} $^7F_0$–$^5L_6$ transition), the emission of CDs@$MgWO_4$: 12%Eu^{3+} nanosheets also enhanced obviously, as shown in Figure S11.

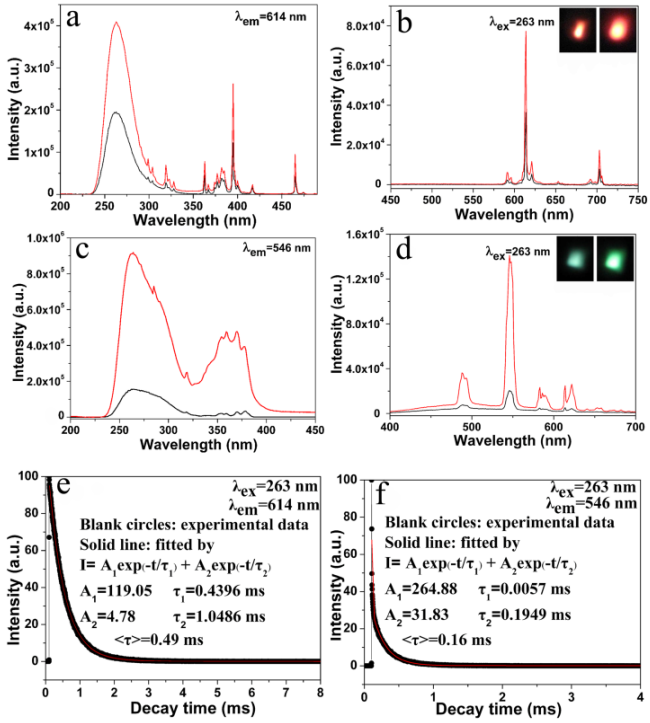

Figure 8. (a) excitation and (b) emission spectra of $MgWO_4$: 12%Eu^{3+} (black line) and CDs@$MgWO_4$: 12%Eu^{3+} (red line) nanosheets, PL (c) excitation and (d) emission spectra of $MgWO_4$: 8%Tb^{3+} (black line) and CDs@$MgWO_4$: 8%Tb^{3+} (red line) nanosheets (Insets are the corresponding luminescence photographs of $MgWO_4$: Ln^{3+} (left) and CDs@$MgWO_4$: Ln^{3+} (right) nanosheets under the irradiation of 263 nm UV light). The luminescent decay curves of (e) CDs@$MgWO_4$: 12%Eu^{3+} and (f) CDs@$MgWO_4$: 8%Tb^{3+} nanosheets.

The luminescent enhancement effect through the incorporation of CDs for $MgWO_4$: Tb^{3+} nanosheets is similar to $MgWO_4$: Eu^{3+} nanosheets. Figure 8c and Figure 8d gave the PL excitation and emission spectra of $MgWO_4$: 8%Tb^{3+} nanosheets (black line) and CDs@$MgWO_4$: 8%Tb^{3+} nanosheets (red line). It can be seen that the excitation and emission intensity of CDs@$MgWO_4$: 8%Tb^{3+} nanosheets are five and seven times stronger than that of $MgWO_4$: 8%Tb^{3+} nanosheets respectively, and the luminescence photograph of CDs@$MgWO_4$: 8%Tb^{3+} nanosheets (insets, right) is brighter compared to $MgWO_4$: 8%Tb^{3+} nanosheets (insets, left) under the irradiation of 263 nm UV light. The corresponding quantum yield is also improved from 6.12% for $MgWO_4$: 8%Tb^{3+} nanosheets to 7.84% for CDs@$MgWO_4$: 8%Tb^{3+} nanosheets. Compared the luminescence enhancement strategy through incorporation of CDs with other methods reported by literatures, such as sensitizing $GdVO_4$: Ln^{3+} (Ln = Dy, Eu) by organic ligands modification (the emission intensity increases about 1.5 folds),[23] forming $CePO_4$: Tb^{3+}/$LaPO_4$ core/shell nanowires (4 folds).[24, 25] It can be seen that the luminescence enhancement through incorporation of CDs is an effective and feasible strategy. In addition, the CDs@$MgWO_4$: Tb^{3+} nanosheets (7 folds) exhibited a higher enhancement than that of CDs@$MgWO_4$: Eu^{3+} nanosheets (2.5 folds) compared to the corresponding samples without incorporation of CDs. According to Dexter's theory, the efficiency of the energy transfer between CDs and Ln^{3+} ion in CDs@$MgWO_4$: Ln^{3+} nanosheets is very sensitive to the energy difference between the excited state energy level of CDs and the energy level of Ln^{3+} ion.[67] Hence, the higher enhancement for CDs@$MgWO_4$: Tb^{3+} nanosheets might be due to the energy difference between the excited state energy level (O π *) of CDs and the energy level of Tb^{3+} ($^5D_4$) could well match the energy required for the transition from CDs to Tb^{3+} ion,[67] which might lead to energy transfer from excited state energy level (O π *) of CDs to Tb^{3+} ($^5D_4$) is preferred to that of CDs to Eu^{3+} ($^5D_0$).

It should be noted that the present results of luminescence enhancement could be further improved through altering the combining conditions such as the amount of CDs, reaction time, combination procedure, etc. For example, the addition amount of CDs solution has obvious effect on the emission intensity of $MgWO_4$: Ln^{3+} nanosheets, as shown in Figure S12. The PL emission intensity of $MgWO_4$: 12%Eu^{3+} nanosheets (Figure S12a) gradually increased with increasing of the amount of CDs solution, and reached maximum at the amount of 0.5 mL. As for $MgWO_4$: 8%Tb^{3+} nanosheets, the PL emission intensity gradually increased with increasing of the amount of CDs solution from 0.1 mL to 1.0 mL (Figure S12b). The luminescent decay curves of CDs@$MgWO_4$: 12%Eu^{3+} and CDs@$MgWO_4$: 8%Tb^{3+} nanosheets were given in Figure 8e and Figure 8f, respectively. These two luminescent decay curves are well fitted into a double exponential function, and the average lifetimes of CDs@$MgWO_4$: 12%Eu^{3+} and CDs@$MgWO_4$: 8%Tb^{3+} nanosheets are 0.49 and 0.16 ms respectively, which are slightly increased compared with the corresponding samples without incorporation of CDs (Figure 2c, 0.39 ms; Figure 2d, 0.10 ms).

To further understand the luminescence enhancement after incorporation of CDs, the PL emission spectra of CDs (black line), $MgWO_4$: 12%Eu^{3+} nanosheets (blue line) and CDs@$MgWO_4$: 12%Eu^{3+} nanosheets (red line) were studied and compared upon the excitation of CDs (λ_{ex} = 440 nm), as shown in Figure S13a. For CDs@$MgWO_4$: 12%Eu^{3+} nanosheets, the emission spectrum is composed of a broad band of CDs and the characteristic sharp lines of Eu^{3+}. However, under the identical excitation conditions, the PL emission spectrum of $MgWO_4$: 12%Eu^{3+} nanosheets only exhibits very weak emission of Eu^{3+}. The similar situation is found in the CDs@$MgWO_4$: 8%Tb^{3+} system, as shown in Figure S13b. This suggests that the CDs could be successfully introduced into $MgWO_4$: Ln^{3+} nanosheets and the energy transfer might be occurred between CDs and $MgWO_4$: Ln^{3+} nanosheets. In addition, the UV−vis diffuse reflectance spectra (DRS) of $MgWO_4$: Ln^{3+} and CDs@$MgWO_4$: Ln^{3+} are shown in Figure S14. It is found that CDs@$MgWO_4$: 12%Eu^{3+} (Figure S14a) and CDs@$MgWO_4$: 8%Tb^{3+} (Figure S14b) nanosheets show an analogous absorption profile in the range of 200−650 nm but stronger absorption intensity compared with the corresponding samples without incorporation of CDs. The energy transfer from CDs to $MgWO_4$: Ln^{3+} in CDs@$MgWO_4$: Ln^{3+} nanosheets could be confirmed by the decay curves of CDs luminescence before and after incorporation onto the $MgWO_4$: Ln^{3+} nanosheets. Figure 9 gives the luminescent decay curves of CDs, CDs@$MgWO_4$: 12%Eu^{3+} and CDs@$MgWO_4$: 8%Tb^{3+} nanosheets. As shown in Figure 9a, the luminescent decay curve of CDs can be well fitted into a single exponential function $I = I_0\exp(-t/\tau)$. According to the fitting calculation, the lifetime value of CDs is about 7.73 ns. As for CDs@$MgWO_4$: 12%Eu^{3+} and CDs@$MgWO_4$: 8%Tb^{3+} nanosheets, the decay curves of CDs luminescence are well fitted into a double exponential function, not a

single exponential function, as shown in Figure 9 (b) and (c) respectively. The double exponential decay behavior is usually observed in the luminescent materials occurred energy transfer phenomenon. Determined by equation (1) and (2), the average lifetimes of CDs luminescence in CDs@$MgWO_4$: 12%Eu^{3+} and CDs@$MgWO_4$: 8%Tb^{3+} nanosheets are about 2.31 and 2.25 ns respectively, which is lower than that of pure CDs, indicating the existence of energy transfer between CDs and $MgWO_4$: Ln^{3+} nanosheets.

The luminescence enhancement mechanism was proposed and discussed according to the energy level structure of WO_4^{2-} group, Eu^{3+}, Tb^{3+}, and CDs. [50,68] The luminescence and energy transfer process in CDs@$MgWO_4$: Ln^{3+} are schematically shown in Figure 10. Upon excitation with 263 nm UV light, the electrons in the ground state ($^1A_1$) are excited into the $^1B(^1T_2)$ level of WO_4^{2-}, where the electrons might relax to its lowest excited $^1B(^1T_2)$ level of WO_4^{2-}, producing the emission by transition to the $^1A_1$ level of WO_4^{2-}. At the same time, the excitation energy in the $^1B(^1T_2)$ level of WO_4^{2-} might transfer to the $^5D_3$ or higher levels of Tb^{3+} by a resonance process for CDs@$MgWO_4$: Tb^{3+} nanosheets. The ener gy levels at $^5D_3$ or higher levels of Tb^{3+} could either be transferred to the $^5D_4$ energy level of the adjacent Tb^{3+} through a cross relaxation process, or be effectively captured by the energy level of CDs and then transferred to $^5D_4$ energy level of Tb^{3+}. Thus, the amount of electrons in $^5D_4$ energy level of Tb^{3+} would be increased and the emission originated from the $^5D_4$ level to ground states of Tb^{3+} ($^7F_6$, $^7F_5$, $^7F_4$ and $^7F_3$) would be enhanced. In addition, the CDs could also be excited by light of certain energy and the electrons are transferred from C π (HOMO) to C π* (LUMO+2) energy level, where either the electrons relax to the lowest excited O π* (LUMO) energy level of CDs with the process of intermediate process (C π*–N π*, and N π*–O π*) by vibration relaxation, producing the emission of CDs by the transition to the C π (HOMO) energy level,[69] or the excitation energy transfers from O π* energy level of CDs to $^5D_4$ energy level of Tb^{3+}, which also results in the enhancement of green emission of Tb^{3+}. As for CDs@$MgWO_4$: Eu^{3+} nanosheets, the excitation energy in the $^1B(^1T_2)$ level of WO_4^{2-} could also transfer to the $^5D_3$ or higher levels of Eu^{3+} by a resonance process, from which the energy could either nonradiatively relax to $^5D_0$ energy level of Eu^{3+} by multiphonon relaxation, or be captured by energy level of CDs and then transferred to $^5D_0$ energy level of Eu^{3+} as well. Simultaneously, an energy transfer from O π* of CDs to $^5D_0$ of Eu^{3+} could be happened through dipole resonance mechanisms. Hence, the amount of electrons in $^5D_0$ energy level of Eu^{3+} would be increased, which leads to the emission enhancement of the transitions from $^5D_0$ to $^7F_1$, $^7F_2$, $^7F_3$ and $^7F_4$ energy levels of Eu^{3+}.

In a word, the mechanism of luminescence enhancement is probably attributed to two factors. The one is that the excited energy level of CDs could efficiently capture the electrons at $^5D_3$ or higher energy levels of Tb^{3+} and Eu^{3+}, and then transfer to the $^5D_4$ energy level of Tb^{3+} and $^5D_0$ energy level of Eu^{3+} respectively, which can effectively reduce the nonradiative transitions from higher energy levels to the lowest excited level of Ln^{3+}. The other one is that the CDs can be excited by light of certain energy and the excitation energy can transfer to $^5D_4$ energy level of Tb^{3+} or $^5D_0$ energy level of Eu^{3+}, which also leads to the enhancement of Tb^{3+} or Eu^{3+} emission.

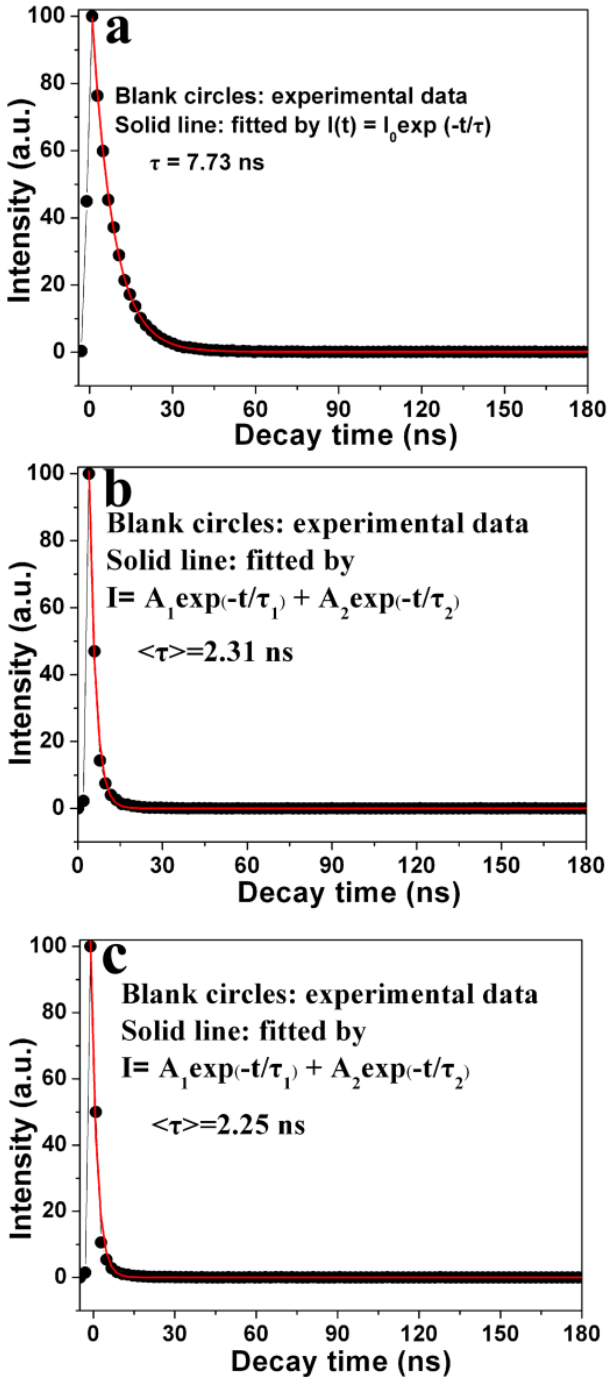

Figure 9. The luminescent decay curves of (a) CDs, (b) CDs@$MgWO_4$: 12%Eu^{3+} and (c) CDs@$MgWO_4$: 8%Tb^{3+} nanosheets under the excitation of 360 nm and monitored at 510 nm (CDs luminescence).

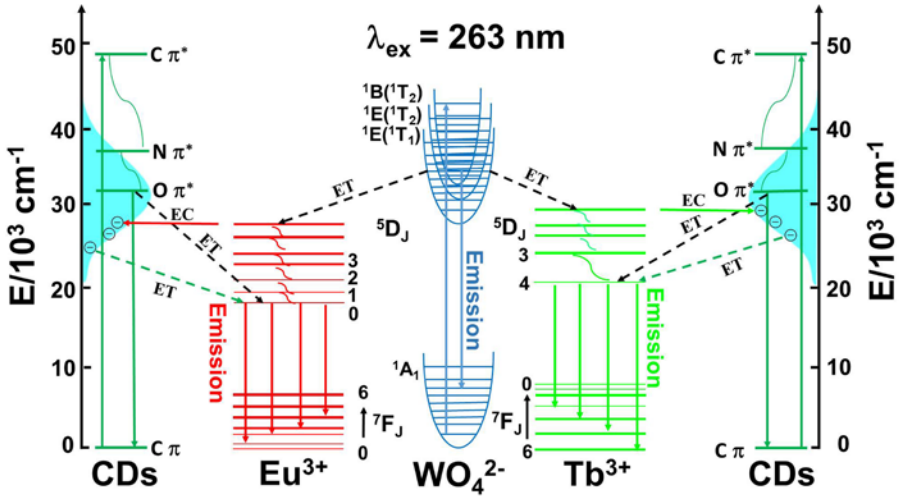

Figure 10. The energy level scheme for CDs@$MgWO_4$: Ln^{3+} (Ln = Tb, Eu) nanosheets. The energy transfer (ET) process from WO_4^{2-}, CDs to Ln^{3+}, electron capture (EC) process of CDs as well as the emission process from Tb^{3+}, Eu^{3+} and CDs.

4. CONCLUSIONS

In conclusion, we developed a simple and environment-friendly strategy to enhance the fluorescence performances of $MgWO_4$: Ln^{3+} (Ln = Eu, Tb) nanosheets through incorporation of CDs to form CDs@$MgWO_4$: Ln^{3+} nanostructures. The morphology and phase structure are almost unaffected after incorporation of CDs onto $MgWO_4$: Ln^{3+} nanosheets, while the emission intensity of CDs@$MgWO_4$: Eu^{3+} and CDs@$MgWO_4$: Tb^{3+} nanosheets increased two and seven folds compared to the corresponding $MgWO_4$: Eu^{3+} and $MgWO_4$: Tb^{3+} samples. The luminescence enhancement mechanism is mainly due to the capture electrons by CDs and energy transfer between CDs and luminescent Ln^{3+}. This investigation not only develops a synthesis procedure of tungstates with 2D structure, but also provides a simple and feasible strategy for improving luminescence property of rare earth ions doped nanomaterials.

ASSOCIATED CONTENT

Supporting Information. Some detailed information on samples are provided in supporting information, including: XRD patterns; SEM, TEM, HRTEM, EDS and SAED images; XPS spectrum; PL spectra and lifetime; UV-Vis DRS. This material is available free of charge via the Internet at http://pubs.acs.org.

AUTHOR INFORMATION

Corresponding Author

*E-mail: liqingf335@163.com.

*E-mail: zlwang2007@hotmail.com.

*E-mail: jinlin_1982@126.com.

*E-mail: jh.hao@polyu.edu.hk.

Author Contributions

The manuscript was written through contributions of all authors. All authors have given approval to the final version of the manuscript. ‡These authors contributed equally.

Notes

The authors declare no competing financial interest.

ACKNOWLEDGMENT

This work is financially supported by the National Natural Science Foundation of China (no. 51572303), the Innovation Scientists and Technicians Troop Construction Projects of Henan Province (no. 2013259), the Program for Innovative Research Team (in Science and Technology) in University of Henan Province (no. 14IRTSTHN009), and Hong Kong RGC GRF (no. PolyU 153281/16P).

REFERENCES

(1) Novoselov, K. S.; Geim, A. K.; Morozov, S. V.; Jiang, D.; Zhang, Y.; Dubonos, S. V.; Grigorieva, I. V.; Firsov, A. A. Electric Field Effect in Atomically Thin Carbon Films. *Science* **2004**, *306*, 666–669.

(2) Bonaccorso, F.; Sun, Z.; Hasan, T.; Ferrari, A. Graphene Photonics and Optoelectronics. *Nat. Photonics* **2010**, *4*, 611–622.

(3) Sun, Y. F.; Sun, Z. H.; Gao, S.; Cheng, H.; Liu, Q. H.; Piao, J. Y.; Yao, T.; Wu, C. Z.; Hu, S. L.; Wei, S. Q.; Xie, Y. Fabrication of Flexible and Freestanding Zinc Chalcogenide Single Layers. *Nat. Commun.* **2012**, *3*, 1057–1063.

(4) Zhu, Y. W.; Murali, S.; Stoller, M. D.; Ganesh, K. J.; Cai, W. W.; Ferreira, P. J.; Pirkle, A.; Wallace, R. M.; Cychosz, K. A.; Thommes, M.; Su, D.; Stach, E. A.; Ruoff, R. S. Carbon-Based Supercapacitors Produced by Activation of Graphene. *Science* **2011**, *332*, 1537–1541.

(5) Zhang, Y.; Tan, Y. W.; Stormer, H. L.; Kim, P. Experimental Observation of Quantum Hall Effect and Berry's Phase in Graphene. *Nature* **2005**, *43*, 201–204.

(6) Geim, A. K.; Novoselov, K. S. The Rise of Graphene. *Nat. Mater.* **2007**, *6*, 183–191.

(7) Chen, Y.; Tan, C. L.; Zhang, H.; Wang, L. Z. Two-Dimensional Graphene Analogues for Biomedical Applications. *Chem. Soc. Rev.* **2015**, *44*, 2681–2701.

(8) Jie, W. J.; Yang, Z. B.; Zhang, F.; Bai, G. X.; Leung, C. X.; Hao, J. H. Observation of Room-Temperature Magnetoresistance in Monolayer MoS_2 by Ferromagnetic Gating. *ACS Nano* **2017**, *11*, 6950–6958.

(9) Bai, G. X.; Yuan, S. G.; Zhao, Y. D.; Yang, Z. B.; Choi, S. K.; Chai, Y.; Yu, S. F.; Lau, S. P.; Hao, J. H. 2D Layered Materials of Rare-Earth Er-Doped MoS_2 with NIR-to-NIR Down- and Up-Conversion Photoluminescence. *Adv. Mater.* **2016**, *28*, 7472–7477.

(10) Butler, S. Z.; Hollen, S. M.; Cao, L. Y.; Cui, Y.; Gupta, J. A.; Gutierrez, H. R.; Heinz, T. F.; Hong, S. S.; Huang, J. X.; Ismach, A. F.; Kuno, M.; Shan, V. V. J.; Shi, L.; Spencer, M. G.; Terrones, M.; Windl, W.; Goldberger, J. E. Progress, Challenges, and Opportunities in Two-Dimensional Materials Beyond Graphene. *ACS Nano* **2013**, *7*, 2898–2926.

(11) Zhang, H. Ultrathin Two-Dimensional Nanomaterials. *ACS Nano* **2015**, *9*, 9451–9469.

(12) Xu, M. S.; Liang, T.; Shi, M. M.; Chen, H. Z. Graphene-Like Two-Dimensional Materials. *Chem. Rev.* **2013**, *113*, 3766–3798.

(13) Yang, Z. B.; Hao, J. H.; Yuan, S. G.; Lin, S. H.; Yau, H. M.; Dai, J. Y.; Lau, S. P. Field-Effect Transistors Based on Amorphous Black Phosphorus Ultrathin Films by Pulsed Laser Deposition. *Adv. Mater*. **2015**, *27*, 3748–3754.

(14) Liu, H.; Du, Y. C.; Deng, Y. X.; Ye, P. D. Semiconducting Black Phosphorus: Synthesis, Transport Properties and Electronic Applications. *Chem. Soc. Rev*. **2015**, *44*, 2732–2743.

(15) Danevich, F. A.; Chernyak, D. M.; Dubovik, A. M. $MgWO_4$–A New Crystal Scintillator. *Nucl. Instrum. Methods Phys. Res.* **2009**, *608*, 107–115.

(16) Pullar, R. C.; Farrah, S.; Alford, N. M. $MgWO_4$, $ZnWO_4$, $NiWO_4$ and $CoWO_4$ Microwave Dielectric Ceramics. *J. Eur. Ceram. Soc*. **2007**, *27*, 1059–1063.

(17) Kim, D. W.; Cho, I. S. Electronic Band Structures and Photovoltaic Properties of MWO_4 (M = Zn, Mg, Ca, Sr) Compounds. *J. Solid State Chem.* **2011**, *184*, 2103–2107.

(18) Feng, X.; Feng, W. L.; Xia, M.; Wang, K.; Liu, H. L.; Deng, D. S.; Qin, X.; Yao, W. K.; Zhu, W. T. Co-Precipitation Synthesis, Photoluminescence Properties and Theoretical Calculations of $MgWO_4$: Eu^{3+} Phosphors. *RSC Adv*. **2016**, *6*, 14826–14831.

(19) Chai, X. N.; Li, J.; Zhang, Y.; Wang, X. S.; Li, Y. X.; Yao, X. Bright Dual-Mode Green Emission and Temperature Sensing Properties in Er^{3+}/Yb^{3+} Co-Doped $MgWO_4$ Phosphor. *RSC Adv*. **2016**, *6*, 64072–64078.

(20) Huang, J. B.; Tian, B. S.; Wang, J.; Wang, Y. B.; Lu, W.; Li, Q. F.; Jin, L.; Li, C. Y.; Wang, Z. L. Controlled Synthesis of 3D Flower-Like $MgWO_4$: Eu^{3+} Hierarchical Structures and Fluorescence Enhancement through Introduction of Carbon Dots. *CrystEngComm* **2018**, *20*, 608–614.

(21) Li, S. W.; Zhang, X.; Hou, Z. Y.; Cheng, Z. Y.; Ma, P. G.; Lin, J. Enhanced Emission of Ultra-Small-Sized LaF_3: RE^{3+} (RE = Eu, Tb) Nanoparticles through 1,2,4,5-Benzenetetracarboxylic Acid Sensitization. *Nanoscale* **2012**, *4*, 5619–5626.

(22) Parchur, A. K.; Prasad, A. I.; Ansari, A. A.; Rai, S. B.; Ningthoujam, R. S. Luminescence Properties of Tb^{3+}-Doped $CaMoO_4$ Nanoparticles: Annealing Effect, Polar Medium Dispersible, Polymer Film and Core–Shell Formation. *Dalton Trans.* **2012**, *41*, 11032–11045.

(23) Song, Y.; Shao, B. Q.; Feng, Y.; Lü, W.; Huo, J. S.; Zhao, S.; Liu, M.; Liu, G. X.; You, H. P. Emission Enhancement and Color Tuning for $GdVO_4$: Ln^{3+} (Ln = Dy, Eu) by Surface Modification at Single Wavelength Excitation. *Inorg. Chem.* **2017**, *56*, 282−291.

(24) Wang, Z. L.; Quan, Z. W.; Jia, P. Y.; Lin, C. K.; Luo, Y.; Chen, Y.; Fang, J.; Zhou, W.; O'Connor, C. J.; Lin, J. A Facile Synthesis and Photoluminescent Properties of Redispersible CeF_3, CeF_3: Tb^{3+}, and CeF_3: Tb^{3+}/LaF_3 (Core/Shell) Nanoparticles. *Chem. Mater*. **2006**, *18*, 2030–2037.

(25) Fang, Y. P.; Xu, A. W.; Dong, W. F. Highly Improved Green Photoluminescence from $CePO_4$: Tb/$LaPO_4$ Core/Shell Nanowires. *Small* **2005**, *1*, 967–971.

(26) Saboktakin, M.; Ye, X. C.; Chettiar, U. K.; Engheta, N.; Murray, C. B.; Kagan, C. R. Plasmonic Enhancement of Nanophosphor Upconversion Luminescence in Au Nanohole Arrays. *ACS Nano* **2013**, *7*, 7186–7192.

(27) Lu, D. W.; Cho, S. K.; Ahn, S.; Brun, L.; Summers, C. J.; Park, W. Plasmon Enhancement Mechanism for the Upconversion Processes in $NaYF_4$: Yb^{3+}, Er^{3+} Nanoparticles: Maxwell versus Förster. *ACS Nano* **2014**, *8*, 7780–7792.

(28) Yin, Z.; Zhou, D. L.; Xu, W.; Cui, S. B.; Chen, X.; Wang, H.; Xu, S. H.; Song, H. W. Plasmon-Enhanced Upconversion Luminescence on Vertically Aligned Gold Nanorod Monolayer Supercrystals. *ACS Appl. Mater. Interfaces* **2016**, *8*, 11667-11674.

(29) Xu, X.; Ray, R.; Gu, Y.; Ploehn, H. J.; Gearheart, L.; Raker, K.; Scrivens, W. A. Electrophoretic Analysis and Purification of Fluorescent Single-Walled Carbon Nanotube Fragments. *J. Am. Chem. Soc.* **2004**, *126*, 12736–12737.

(30) Xie, Z.; Wang, F.; Liu, C. Y. Organic–Inorganic Hybrid Functional Carbon Dot Gel Glasses. *Adv. Mater.* **2012**, *24*, 1716–1721.

(31) Shi, W.; Li, X.; Ma, H. A. Tunable Ratiometric pH Sensor Based on Carbon Nanodots for the Quantitative Measurement of the Intracellular pH of Whole Cells. *Angew. Chem. Int. Ed*. **2012**, *124*, 6538–6541.

(32) Shen, L.; Zhang, L.; Chen, M.; Chen, X.; Wang, J. The Production of pH-Sensitive Photoluminescent Carbon Nanoparticles by the Carbonization of Polyethylenimine and Their Use for Bioimaging. *Carbon* **2013**, *55*, 343–349.

(33) De, B.; Voitb, B.; Karak, N. Carbon Dot Reduced Cu_2O Nanohybrid/Hyperbranched Epoxy Nanocomposite: Mechanical, Thermal and Photocatalytic Activity. *RSC Adv.* **2014**, *4*, 58453–58459.

(34) Choi, H.; Ko, S. J.; Choi, Y.; Joo, P.; Kim, T.; Lee, B.; Jung, J. W.; Choi, H. J.; Cha, M.; Jeong, J. R.; Hwang, I. W.; Song, M. H.; Kim, B. S.; Kim, J. Y. Versatile Surface Plasmon Resonance of Carbon-Dot-Supported Silver Nanoparticles in Polymer Optoelectronic Devices. *Nat. Photonics* **2013**, *7*, 732–738.

(35) Gogoi, N.; Devasish, C. H. Novel Carbon Dot Coated Alginate Beads with Superior Stability, Swelling and pH Responsive Drug Delivery. *J. Mater. Chem. B* **2014**, *2*, 4089–4099.

(36) Li, H. T.; He, X. D.; Kang, Z. H.; Liu, Y.; Liu, J. L.; Lian, S. Y.; Tsang, C. H. A.; Yang, X. B.; Lee, S. T. Water-Soluble Fluorescent Carbon Quantum Dots and Photocatalyst Design. *Angew. Chem. Int. Ed*. **2010**, *49*, 4430–4434.

(37) Cao, L.; Sahu, S.; Anilkumar, P.; Bunker, C. E.; Xu, J.; Fernando, K. A. S.; Wang, P.; Guliants, E. A.; Tackett, K. N.; Sun, Y. P. Carbon Nanoparticles as Visible-Light Photocatalysts for Efficient CO_2 Conversion and Beyond. *J. Am. Chem. Soc.* **2011**, *133*, 4754–4757.

(38) Ming, H.; Yan, Y. R.; Ming, J.; Li, X. W.; Zhou, Q.; Huang, H.; Zheng, J. W. Porous TiO_2 Nanoribbons and TiO_2 Nanoribbon/Carbon Dot Composites for Enhanced Li-Ion Storage. *RSC Adv.* **2014**, *4*, 12971–12976.

(39) Hu, J.; Zou, C.; Su, Y. J.; Li, M.; Hu, N. T.; Ni, H.; Yang, Z.; Zhang, Y. F. Enhanced NO_2 Sensing Performance of Reduced Graphene Oxide by in-situ Anchoring Carbon dots. *J. Mater. Chem. C* **2017**, *10*, 1039–1049.

(40) Atkin, P.; Daeneke, T.; Wang, Y.; Carey, B. J.; Berean, K. J.; Clark, R. M.; Ou, J. Z.; Trinchi, A.; Cole, I. S.; Kalantar, K. 2D WS_2/Carbon Dot Hybrids with Enhanced Photocatalytic Activity. *J. Mater. Chem. A* **2016**, *4*, 13563–13571.

(41) De, B.; Voit, B.; Karak, N. Transparent Luminescent Hyperbranched Epoxy/Carbon Oxide Dot Nanocomposites with Outstanding Toughness and Ductility. *ACS Appl. Mater. Interfaces* **2013**, *5*, 10027–10034.

(42) Bai, G. X.; Tsang, M. K.; Hao, J. H. Luminescent Ions in Advanced Composite Materials for Multifunctional Applications. *Adv. Funct. Mater.* **2016**, *26*, 6330–6350.

(43) Samanta, T.; Hazra, C.; Mahalingam, V. C-Dot Sensitized Eu^{3+} Luminescence from Eu^{3+}-Doped LaF_3–C Dot Nanocomposites. *New J. Chem.* **2015**, *39*, 106–109.

(44) Zhu, S. J.; Meng, Q. N.; Wang, L.; Zhang, J. H.; Song, Y. B.; Jin, H.; Zhang, K.; Sun, H. C.; Wang, H. Y.; Yang, B. Highly Photoluminescent Carbon Dots for Multicolor Patterning, Sensors, and Bioimaging. *Angew. Chem. Int. Ed.* **2013**, *52*, 3953–3957.

(45) Su, Y. G.; Li, L. P.; Li, G. S. Synthesis and Optimum Luminescence of $CaWO_4$-Based Red Phosphors with Codoping of Eu^{3+} and Na^+. *Chem. Mater*. **2008**, *20*, 6060–6067.

(46) Yue, D.; Li, Q. F.; Lu, W.; Wang, Q.; Wang, M. N.; Wang, Z. L.; Hao, J. H. Multi-Color Luminescence of Uniform $CdWO_4$ Nanorods through Eu^{3+} Ion Doping. *J. Mater. Chem. C* **2015**, *3*, 2865–2871.

(47) Tian, Y.; Chen, B. J.; Hua, R. N.; Yu, N. S.; Liu, B. Q.; Sun, J. S.; Cheng, L. S.; Zhong, H. Y.; Li, X. P.; Zhang, J. S.; Tian, B. N.; Zhong, H. Self-Assembled 3D Flower-Shaped $NaY(WO_4)_2$: Eu^{3+} Microarchitectures: Microwave-Assisted Hydrothermal Synthesis, Growth Mechanism and Luminescent Properties. *CrystEngComm* **2012**, *14*, 1760–1769.

(48) Tian, Y.; Qi, X. H.; Wu, X. W.; Hua, R. N.; Chen, B. J. Luminescent Properties of $Y_2(MoO_4)_3$: Eu^{3+} Red Phosphors with FlowerLike

Shape Prepared via Coprecipitation Method. *J. Phys. Chem. C* **2009**, *113*, 10767–10772.

(49) Yue, D.; Lu, W.; Jin, L.; Li, C. Y.; Luo, W.; Wang, M. N.; Wang, Z. L.; Hao, J. H. Controlled Synthesis, Asymmetrical Transport Behavior and Luminescence Properties of Lanthanide Doped ZnO Mushroom-Like 3D Hierarchical Structures. *Nanoscale* **2014**, *6*, 13795–13802.

(50) Wang, W. X.; Yang, P. P.; Cheng, Z. Y.; Hou, Z. Y.; Li, C. X.; Lin, J. Patterning of Red, Green, and Blue Luminescent Films Based on $CaWO_4$: Eu^{3+}, $CaWO_4$: Tb^{3+}, and $CaWO_4$ Phosphors via Microcontact Printing Route. *ACS Appl. Mater. Interfaces* **2011**, *3*, 3921-3928.

(51) Yue, D.; Lu, W.; Li, C. Y.; Luo, W.; Zhang, X. L.; Liu, C. X.; Wang, Z. L. Controllable Synthesis of Ln^{3+} (Ln = Tb, Eu) Doped Zinc Phosphate Nano-/Micro-Structured Materials: Phase, Morphology and Luminescence Properties. *Nanoscale* **2014**, *6*, 2137–2145.

(52) Wang, Z. L.; Hao, J. H.; Chan, H. L. W. Down- and Up-Conversion Photoluminescence, Cathodoluminescence and Paramagnetic Properties of $NaGdF_4$: Yb^{3+}, Er^{3+} Submicron Disks Assembled from Primary Nanocrystals. *J. Mater. Chem.* **2010**, *20*, 3178–3185.

(53) Puvvada, N.; Kumar, B. N. P.; Konar, S.; Kalita, H.; Mandal, M.; Pathak, A. Synthesis of Biocompatible Multicolor Luminescent Carbon Dots for Bioimaging Applications. *Sci. Technol. Adv. Mater.* **2012**, *13*, 045008.

(54) Ding, H.; Yu, S. B.; Wei, J. S.; Xiong, H. M. Full-Color Light-Emitting Carbon Dots with a Surface-State-Controlled Luminescence Mechanism. *ACS Nano* **2016**, *10*, 484−491.

(55) Dong, Y. Q.; Pang, H. C.; Yang, H. B.; Guo, C. X.; Shao, J. W.; Chi, Y. W.; Li, C. M.; Yu, T. Carbon-Based Dots Co-Doped with Nitrogen and Sulfur for High Quantum Yield and Excitation-Independent Emission. *Angew. Chem. Int. Ed.* **2013**, *52*, 7800–7804.

(56) Zhang, W. F.; Jin, L. M.; Yu, S. F.; Zhu, H.; Pan, S. S.; Zhao, Y. H.; Yang, H. Y. Wide-Bandwidth Lasing from C-dot/Epoxy Nano Composite Fabry–Perot Cavities with Ultralow Threshold. *J. Mater. Chem. C* **2014**, *2*, 1525–1531.

(57) Gao, X. H.; Lu, Y. Z.; Zhang, R. Z.; He, S. J.; Ju, J.; Liu, M. M.; Li, L.; Chen, W. One-Pot Synthesis of Carbon Nanodots for Fluorescence Turn-on Detection of Ag^+ Based on the Ag^+-Induced Enhancement of Fluorescence. *J. Mater. Chem. C* **2015**, *3*, 2302–2309.

(58) Xu, X. Y.; Yan, B. Fabrication and Application of a Ratiometric and Colorimetric Fluorescent Probe for Hg^{2+} Based on Dual-Emissive Metal–Organic Framework Hybrids with Carbon Dots and Eu^{3+}. *J. Mater. Chem. C* **2016**, *4*, 1543–1549.

(59) Zu, Y. Q.; Zhang, Y.; Xu, K. Z.; Zhao, F. Q. A Graphene Oxide–$MgWO_4$ Nanocomposite as an Efficient Catalyst for the Thermal Decomposition of RDX, HMX. *RSC Adv.* **2016**, *6*, 31046–31052.

(60) Zheng, Y. H.; Lin, J. T.; Wang, Q. M. Emissions and Photocatalytic Selectivity of $SrWO_4$: Ln^{3+} (Eu^{3+}, Tb^{3+}, Sm^{3+} and Dy^{3+}) Prepared by a Supersonic Microwave Co-Assistance Method. *Photochem. Photobiol. Sci.* **2012**, *11*, 1567–1574.

(61) Krishnamoorthy, K.; Veerapandian, M.; Yun, V. K.; Kim, S. J. The Chemical and Structural Analysis of Graphene Oxide with Different Degrees of Oxidation. *Carbon* **2013**, *53*, 38–49.

(62) Gao, Y.; Liu, L. Q.; Zu, S. Z.; Peng, K.; Zhou, D.; Han, B. H.; Zhang, Z. The Effect of Interlayer Adhesion on the Mechanical Behaviors of Macroscopic Graphene Oxide Papers. *ACS Nano* **2011**, *5*, 2134–2141.

(63) Shen, Y.; Wu, Y. B.; Li, X. Y.; Zhao, Q. D.; Hou, Y. One-Pot Synthesis of $MgFe_2O_4$ Nanospheres by Solvothermal Method. *Mater. Lett.* **2013**, *96*, 85–88.

(64) Kumar, B. V.; Prasad, M. D.; Vithal, M. Enhanced Visible Light Photocatalytic Activity of Sn Doped Bi_2WO_6 Nanocrystals. *Mater. Lett.* **2015**, *152*, 200–202.

(65) Gupta, S. K.; Sahu, M.; Ghosh, P. S.; Tyagi, D.; Saxen, M. K.; Kadama, R. M. Energy Transfer Dynamics and Luminescence Properties of Eu^{3+} in $CaMoO_4$ and $SrMoO_4$. *Dalton Trans.* **2015**, *44*, 18957–18969.

(66) Bhunia, S. K.; Pradhan, N.; Jana, N. R. Vitamin B Derived Blue and Green Fluorescent Carbon Nanoparticles for Cell-Imaging Application. *ACS Appl. Mater. Interfaces* **2014**, *6*, 7672–7679.

(67) Liu, D.; Wang, Z. G.; Yu, H.; You, J. Fluorescence Properties of Novel Rare Earth Complexes Using Carboxyl-Containing Polyaryletherketones as Macromolecular Ligands. *Eur. Polym. J.* **2009**, *45*, 2260–2268.

(68) Tang, L.; Ji, R.; Li, X.; Teng, K. S.; Lau, S. P. Energy-Level Structure of Nitrogen-Doped Graphene Quantum Dots. *J. Mater. Chem. C* **2013**, *1*, 4908–4915.

(69) Suzuki, K.; Malfatti, L.; Carboni, D.; Loche, D.; Casula, M.; Moretto, A.; Maggini, M.; Takahashi, M.; Innocenzi, P. Energy Transfer Induced by Carbon Quantum Dots in Porous Zinc Oxide Nanocomposite Films. *J. Phys. Chem. C* **2015**, *119*, 2837–2843.